

Electronic Supplementary Information:

Redox-active oxide molten salt composites as a new family of high-capacity thermal energy storage materials

Hilal Bektas¹, Runxia Cai^{1,†}, Saqlain Raza², Jun Liu², Fanxing Li^{1*}

¹ *Department of Chemical and Biomolecular Engineering, North Carolina State University, 911 Partners Way, Raleigh, North Carolina 27695, USA*

² *Department of Mechanical and Aerospace Engineering, North Carolina State University, Raleigh, North Carolina 27695, USA*

**Corresponding author, fli5@ncsu.edu*

1. Experimental Methods:

1.1 Material Preparation:

Sol-gel Method:

Some of the perovskite oxides were synthesized by using a modified Pechini method.¹ First, stoichiometric amounts of nitrate-based precursors were added with 5 ml of deionized water in a beaker, followed by adding citric acid with a molar ratio of 2.5:1 (citric acid:precursors) and another 25 ml of deionized water. The solution was stirred at 300 rpm for 30 min on a hotplate at 40°C. After that, ethylene glycol was added to the solution with a molar ratio of 1.5:1 (ethylene glycol:citric acid) to form a mixture in the gel form. The solution was stirred for 3-4 hours at 80°C till a gel-like mixture is obtained. The resulting mixture was dried at 130 °C overnight. This was followed by calcination in a muffle furnace at 1000 °C for 10 hours to form the perovskite phase. Ca₂AlMnO_{5+δ} was first pre-calcined at 450 °C for 3 hours, then calcined at 1250 °C for 24 h in a tube furnace, with the first 12 hours in air and the remaining 12 hours in a N₂ atmosphere.

Composite Material Preparation:

Metal oxides and salt mixtures were mixed and ground in a mortar. Then, a small portion of the particles was separated for TGA-DSC experiments, and the rest of the powders were pelletized in a 6 mm I.D. pellet dies at 10 MPa for 5 min with a hydraulic press. This was followed by sintering in a muffle furnace at a temperature 50 °C above the melting point of the salt. This step was to ensure the uniform mixing of the salt and perovskite within a liquid phase. For example, a composite material that includes eutectic salt NaF-CaF₂ with a melting point of 810 °C was sintered under the following heating procedure: heating up to 710 °C from room temperature at a heating rate of 3 °C/min, then to 860 °C at a rate of 1 °C/min, and holding at 860 °C for 1 h. This was followed by cooling down to room temperature at a heating rate of 3 °C/min. Then, the pellets were crushed into fine particles for XRD analysis.

For thermal conductivity measurements, two identical pellets were created for LSF1, LiF-NaF-CaF₂, and the composite material LSF1:LiF-NaF-CaF₂. LiF-NaF-CaF₂ was produced by mixing individual salts with 15 grams of 3 mm balls in a high-energy ball mill for 1 hour. To prepare the composite material, the salt mixture was combined with salt-grinded LSF1 in a mortar with the salt:oxide weigh ratio of 0.6:0.4. The powders were pelletized in 30 mm I.D. pellet dies at 40 MPa for 1 hour. Due to its fragile structure, the pelletizing duration for LSF1 was increased to 2 hours, and the sample was calcined at 1000°C for 3 hours to improve the pellet strength.

1.2 TGA-DSC Analysis:

The second cycles were used for the determination of melting/crystallization enthalpy and temperature since the first cycles, which removed the effects of thermal history, were not representative.^{2,3} Melting/crystallization enthalpy was calculated using a linear baseline method. The total energies obtained from integration were divided by the sample weight at the onset of the phase transition. Melting temperature was determined from the onset temperature which is the intersection of the extrapolated baseline with the leading edge, while the crystallization point was identified as the temperature where the heat flow curved deviates from the horizontal baseline.⁴

For SCFM2:NaF-CaF₂, the reduction and oxidation capacities of SCFM2 were determined from the weight changes (%) during gas switches in each cycle. Assuming equal salt evaporation during both ramp-up (reduction) and ramp-down (oxidation) steps, the total weight loss per cycle was found by calculating the difference between the weight at the start and end of each cycle. Oxidation capacity was corrected by adding half of this weight loss while reduction capacity was adjusted by subtracting the other half. For the first 10 cycles, mean values and standard error bars, obtained from three repeated measurements, were provided in Figure 3b. Due to large error bars in the 3rd cycle, possibly caused by the buoyancy forces during the first gas switching, the results are provided starting from the 4th cycle. Error bars decayed in the following cycles, suggesting that the effect of buoyancy forces diminished over time.

1.3 Estimation of Overall Energy Storage Density:

The total energy storage density of composite materials, ΔH_{total} (kJ/kg), including latent heat, thermochemical heat, and sensible heat can be calculated as follows:

$$\Delta H_{total} = w_s \left(\Delta H_{latent} + \int_{T_l}^{T_m} C_s dT + \int_{T_m}^{T_u} C_l dT \right) + w_o \left(\Delta H_{chem} + \int_{T_l}^{T_u} C_o dT \right)$$

where ΔH_{latent} (kJ/kg_{salt}), and ΔH_{chem} (kJ/kg_{oxide}), are respectively latent and thermochemical energy densities. T_l and T_u represent upper and lower temperature limits (K) and T_m is the melting temperature (K). C_s and C_l are the heat capacities of salt in solid and liquid phases (kJ/kg/K), respectively while C_o is the heat capacity of oxide (kJ/kg/K). w_s and w_o denote the mass fractions of salt and oxide, respectively.

ΔH_{latent} was obtained from the TGA-DSC experiments as described above. A maximum of 10% deviation (provided as percentage error bar) was obtained between repeated measurements. Melting enthalpies were used as the latent heat in the determination of overall energy density since the accuracy in the measurement of crystallization enthalpy can be affected by factors such as supercooling or fast heat dissipation.⁴ For example, in the case of LSF1: Li₂MoO₄, the solidification peak was not even formed (Figure S26,27, and 31) even though the endothermic peaks in subsequent cycles indicate the melting of Li₂MoO₄.

Thermochemical energy density, ΔH_{chem} (kJ/kg_{oxide}) for SCFM2:NaF-CaF₂ can be determined by integrating partial molar enthalpy over a specific range of non-stoichiometry, as described in our previous study.⁵ In that study, we used the Van't Hoff method to determine partial molar enthalpy changes at various non-stoichiometry levels. Here, we calculated ΔH_{chem} using our previously obtained enthalpy data over the nonstoichiometric range corresponding to the weight changes of SCFM2 in each cycle. For redox cycling of SCFM2:NaF-CaF₂, DSC does not provide a reliable estimation for ΔH_{chem} since limited heat transfer from continuous oxygen

exchange over time limits the sensitivity of the DSC method. However, for LSF1: Li_2MoO_4 , thermochemical energy density, ΔH_{chem} was determined from DSC measurement using the exothermic peak observed during oxidation. The rapid heat transfer from fast oxidation ensures that DSC is reliable in that case.

Sensible heat was found based on the estimated heat capacities of oxide and salt. The heat capacity of SCFM2 and LSF1 at high temperatures were approximated as 0.84 and 0.54 kJ/(kg·K), respectively, using the equation of $C_p = 3 R n_{atom} / M_{oxide}$ as in the study of Imponenti et al.⁶ To estimate the heat capacity of molten salts mixtures, we used the additive principle, which is commonly used in the literature.^{7,8} For chloride salts, this method showed a maximum deviation of 11% from the experimental data.⁸ The sensible heat for NaF-CaF₂ and LiF-NaF-CaF₂ was calculated using the Shomate equation constants of individual salts from the NIST database.⁹ The equations for the solid phase were integrated from the lower temperature limit to the melting point and the equations for the liquid phase were integrated from the melting point to the upper temperature. Dulong-Petit method, another common approach for the estimation heat of capacity of alkali fluoride salts^{8,10}, resulted in sensible heat values of up to 12% higher than the additive method. Even though the Dulong-Petit method was considered a good method, it does not account for temperature dependence. For Li_2MoO_4 , sensible heat was estimated as ~ 86 kJ/kg_{salt} by additive principle using the NIST database on Li_2O and MoO_3 . For a similar structure, $\text{Li}_2\text{W}_{1-0.0125}\text{Mo}_{0.0125}\text{O}_4$, the sensible heat was calculated as ~ 104 kJ/kg_{salt} over the same temperature range, based on experimental data from the study of Matskevich et al.¹¹

1.4 Thermal Conductivity Measurements:

Thermal conductivity measurements were performed using a 13.2 mm diameter C-Therm Hot Disc sensor, which consists of nickel encapsulated within Kapton. In this study, the samples with a diameter of 30 mm and a thickness of ~ 4 mm can be considered thin slabs. For each measurement, identical pellets were placed on both sides of the sensor, with foam as a background material to satisfy the semi-infinite boundary condition.¹² During the measurement, a compression stand maintained uniform contact between the foam, the samples, and the sensor. The power supply was controlled using the C-Therm software, and the average temperature increase for the sensor was measured. The measurements were repeated 3 times.

The temperature increase was fitted using the Ansys Transient Thermal model. Similar models have been used for bulk and thin film materials.¹²⁻¹⁴ The extremity boundaries of the model were thermally insulated. The power input to the nickel heater and simulation time were set to match the experimental conditions to ensure consistency. Then, the volume-average temperature increase of the nickel was obtained. The thermal conductivity of each sample was determined based on the established thermal properties of nickel, Kapton, and foam as well as the measured density and specific heat capacity of the samples at room temperature. The density of the pellets was measured as 4.6, 2.08, and 2.82 g/cm³ for LSF1, LiF-NaF-CaF₂, and LSF1:LiF-NaF-CaF₂, respectively. A heat capacity of 0.4 kJ/kg-K was used for LSF1 based on the literature values of similar perovskite oxides at room temperature.^{15,16} The heat capacities of LiF-NaF-CaF₂ and LSF1:LiF-NaF-CaF₂ were estimated as 1.23 and 0.92 kJ/kg-K, respectively using the additive principle and NIST database.⁹ Error bars of the thermal conductivity measurements were up to 15%.

2. Relative stability of the fluoride salts:

Table S1 shows the relative stability of fluoride phases in selected chemical spaces with 3 elements. The stabilities were assessed by comparing the DFT-calculated formation energies from phase diagrams generated using Material's project.¹⁷ While this practical approach offers

a useful guideline for understanding the instability issues, it has specific limitations. First, a chemical space including 3 elements is not representative of the real system. A more accurate prediction would require considering a broader chemical space including all the relevant elements to account for the thermodynamic favorability of oxide phases in addition to fluorides. In such chemical space, formation energies of all identified phases need to be included. The complexity of formed phases requires additional DFT calculations for the formation energies of such phases since they may not be included in the Materials Project's database. In addition, a more accurate stability analysis should use a convex hull analysis by evaluating how much a material's energy can be reduced by decomposing into more stable competing phases.¹⁸ While such complex analysis is beyond the scope of this study, it can provide valuable guidance for the future design of ROMS composites.

Table S1. Relative stability of fluoride phases based in selected chemical spaces based on DFT formation energies (eV/atom) *These results are obtained from Materials Project's database and phase diagram tool*¹⁷

Chemical Space	Stability Comparison
Ca-Li-F	CaF ₂ (-4.224)>LiF (-3.166)
Sr-Li-F	SrF ₂ (-4.233)>LiF (-3.166)
Li-Na-F	LiF (-3.166)>NaF (-2.939)
Ca-Na-F	CaF ₂ (-4.224)>NaF (-2.939)
La-Li-F	LaF ₃ (-4.492)>LiF (-3.166)
K-Ca-F	CaF ₂ (-4.224)>KCaF ₃ (-3.725)>KF (-2.936)
K-Na-F	NaF (-2.939)> KF (-2.936)

3. TGA-DSC Results:

Regarding SCFM2:NaF-NaCl, significant weight loss (16.6 wt.%) was observed, which caused a dramatic decrease in the heat of fusion of NaF-NaCl over 4 cycles as presented in Figure S9. This can be attributed to the high vapor pressure of NaCl and the evaporation of the molten salt at high temperatures.¹⁹ The heat of fusion and melting peak point were determined as ~341 kJ/kg_{salt} and ~672 °C while the theoretical values are 572 kJ/kg_{salt} and 675 °C²⁰, respectively. No O₂ uptake was obtained from SCFM2. These results can be explained by chemical interactions between NaF-NaCl and SCFM2 during the experiment. Even though the sample was found to be compatible, phase segregation in both perovskite and salt phases might have occurred during 4 cycles in this experiment. This would also explain the mismatch between the measured and theoretical heat of fusion and melting point.

The measurement for LSF1: Li₂CO₃-Na₂CO₃, was conducted in a 50%CO₂/50%Ar atmosphere as previous research indicated carbonate salts can be more stable in a CO₂ atmosphere.²¹ The heat of fusion was measured as ~239 kJ/kg_{salt} which was lower than the theoretical heat of fusion (370 kJ/kg_{salt}). That might indicate the decomposition of carbonated salt even though 50% CO₂ was introduced into the atmosphere. On the other hand, Figure S25 shows that the peaks corresponding to the phase change of MgF₂-NaF-CaF₂ completely disappeared in a few cycles. In the compatibility test via XRD analysis, a peak that indicates an interaction between LSF1 and LiF-NaF-MgF₂ was not seen. However, the phase of MgF₂ was also not seen in the XRD pattern (see Figure 3b). This was either caused by the small fraction of MgF₂ or its evaporation during the sintering. The latter possibility can also be supported by the heat flow

measurement as the disappearance of the peak might be explained by the degradation of the eutectic phase of $\text{MgF}_2\text{-NaF-CaF}_2$ (Figure S25a).

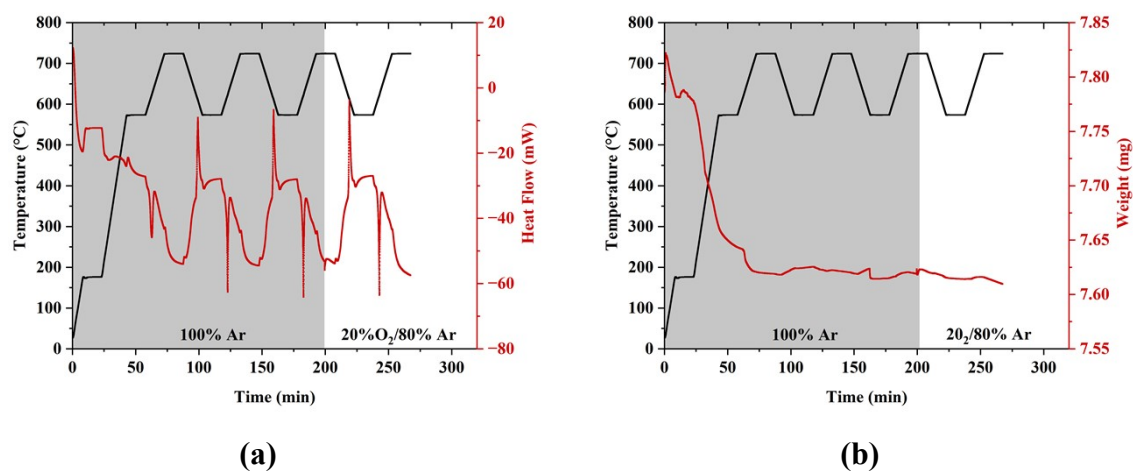


Figure S1. TGA-DSC Measurements for SF:LiF-NaF with the weight ratio of 0.5:0.5 at 550-750 °C (a) Heat Flow (mW) (b) Weight (mg)

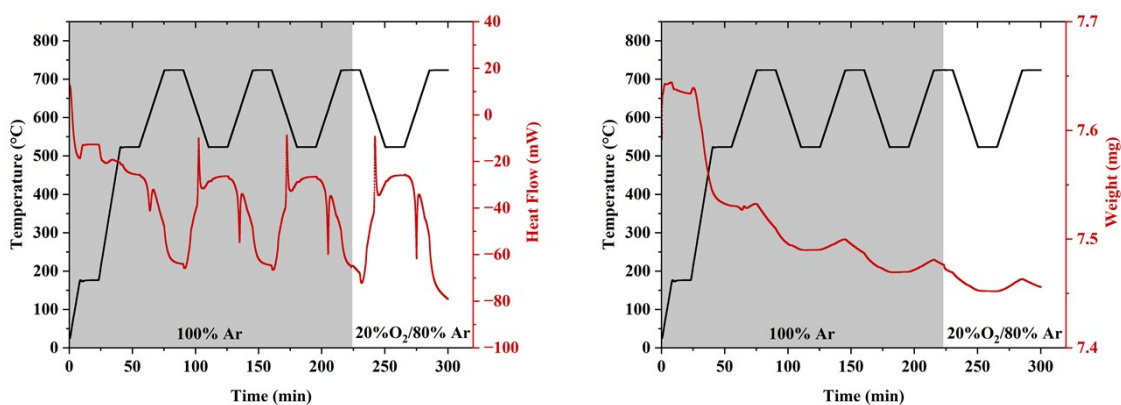
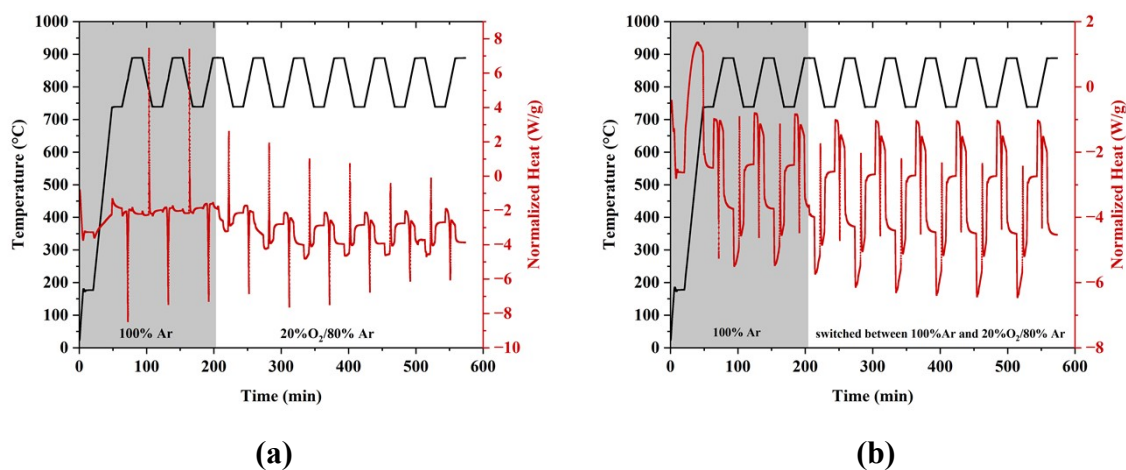
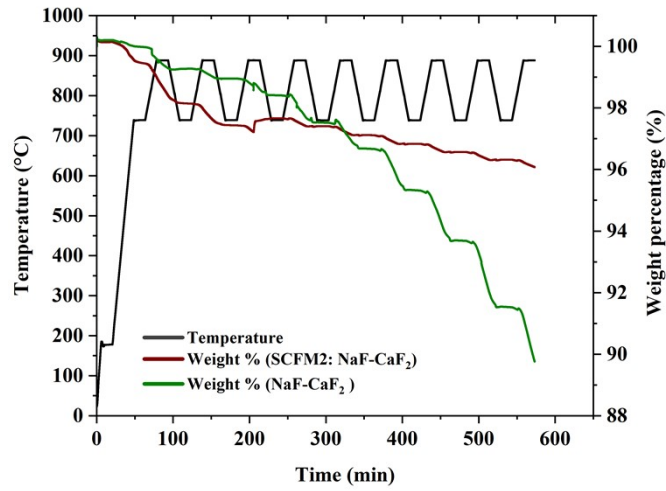


Figure S2. TGA-DSC Measurements for SBF:LiF-NaF with the weight ratio of 0.5:0.5 at 575-725 °C (a) Heat Flow (mW) (b) Weight (mg)





(c)

Figure S3. TGA-DSC Measurements for NaF-CaF₂ and SCFM2: NaF-CaF₂ with the weight ratio of 0.4:0.6 at 740-890 °C (a) Normalized heat flow (W/g) for NaF-CaF₂ (b) Normalized heat flow (W/g) for SCFM2: NaF-CaF₂ (c) Comparison of weight percentages

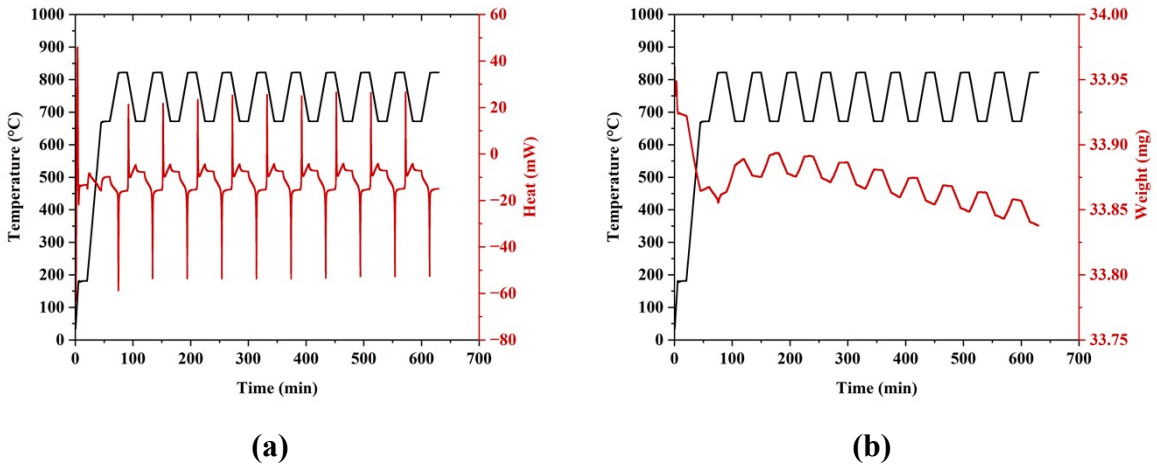


Figure S4. TGA-DSC Measurements for NaF-CaF₂ at 670-820 °C under 100% Ar (a) Heat Flow (mW) (b) Weight (mg) *Weight (mg) represent the total weight of NaF-CaF₂ (~4.35 mg) and inert material YSZ (~29.5 mg)*

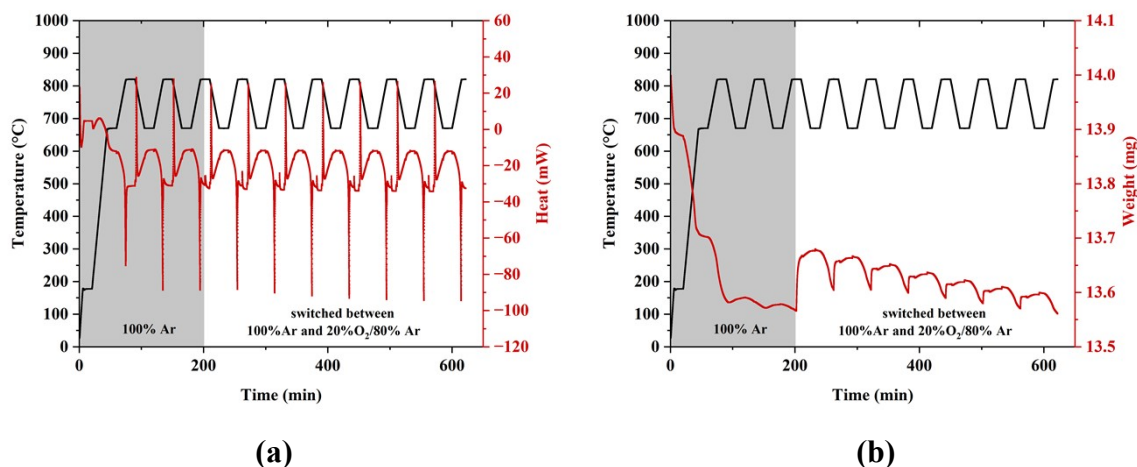


Figure S5. TGA-DSC Measurements for SCFM2: NaF-CaF₂ with the weight ratio of 0.4:0.6 at 670/20%O₂-820 °C/Ar (a) Heat flow (mW) (b) Weight (mg)

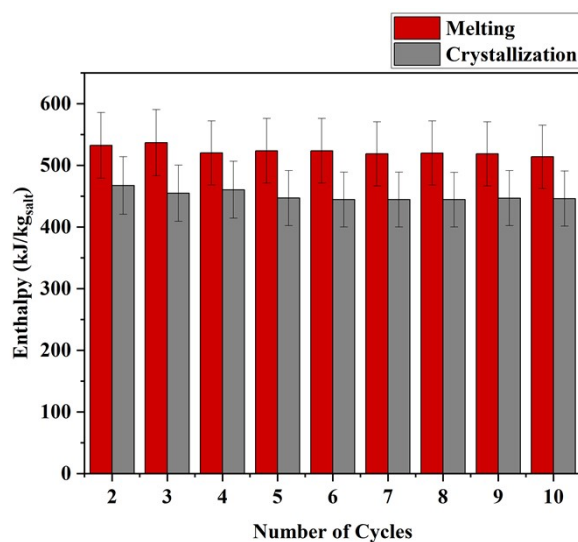


Figure S6. Melting and crystallization enthalpy for SCFM2:NaF-CaF₂ with the weight ratio of 0.4:0.6 at 670°C/20% O₂-820°C/Ar during 10 cycles

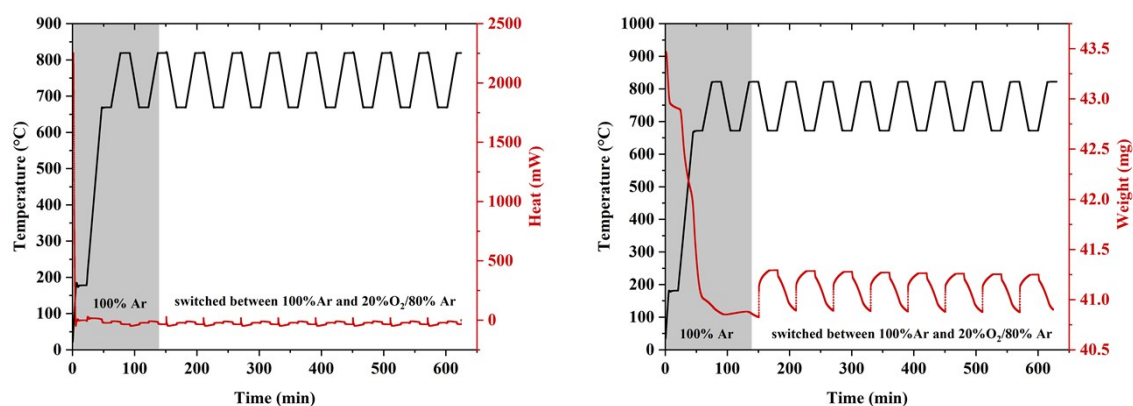


Figure S7. TGA-DSC Measurements for SCFM2 with the weight ratio of 0.4:0.6 at 670/20%O₂-820 °C/Ar (a) Heat flow (mW) (b) Weight (mg)

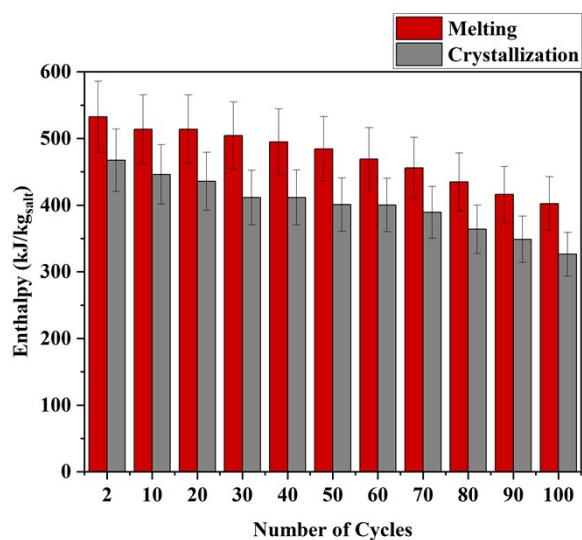


Figure S8. Melting and crystallization enthalpy for SCFM2:NaF-CaF₂ with the weight ratio of 0.4:0.6 at 670°C/20% O₂-820°C/Ar during 100 cycles

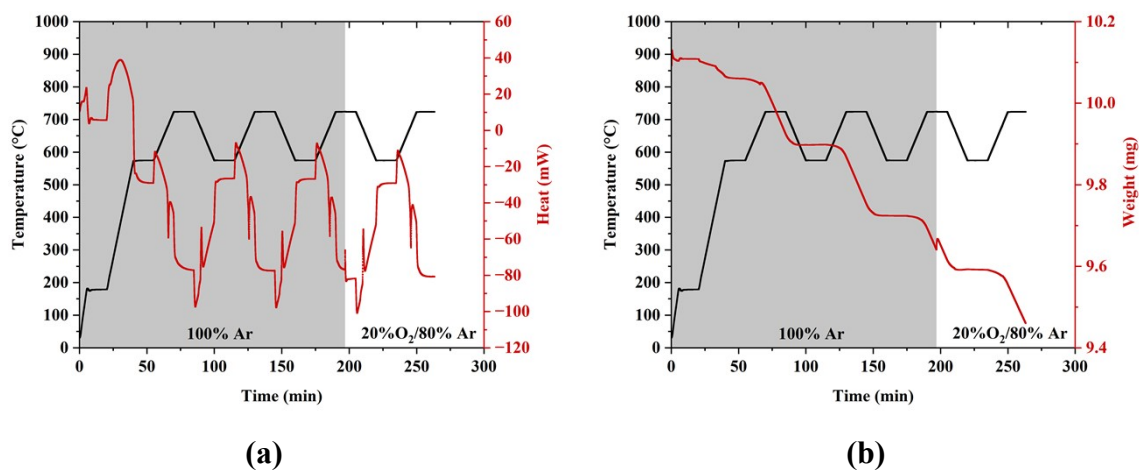
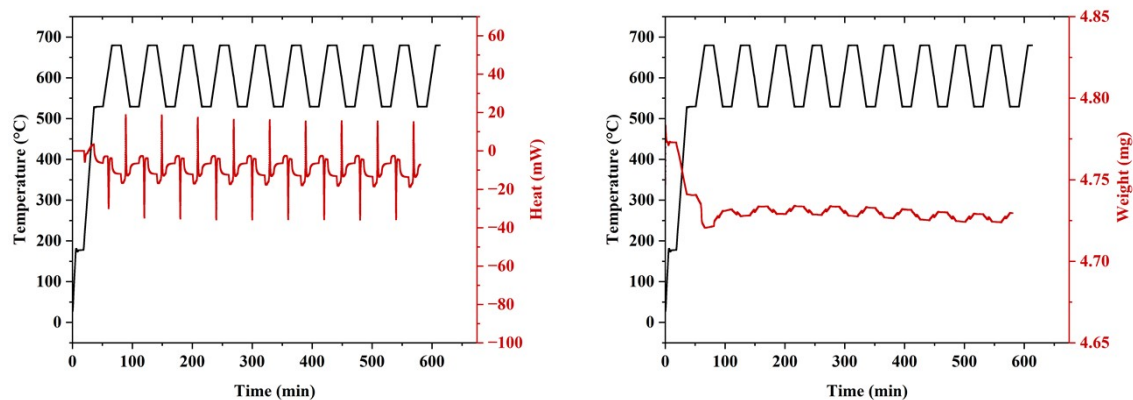


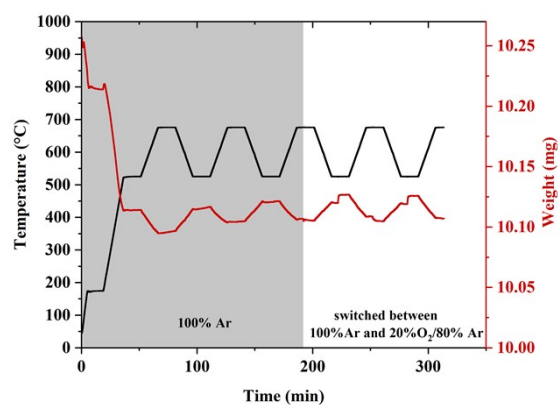
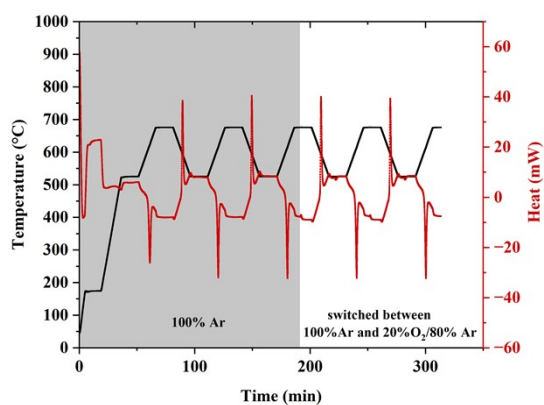
Figure S9. TGA-DSC Measurements for SCFM2: NaF-NaCl with the weight ratio of 0.5:0.5 at 575/20%O₂-725 °C/Ar (a) Heat Flow (mW) (b) Weight (mg)



(a)

(b)

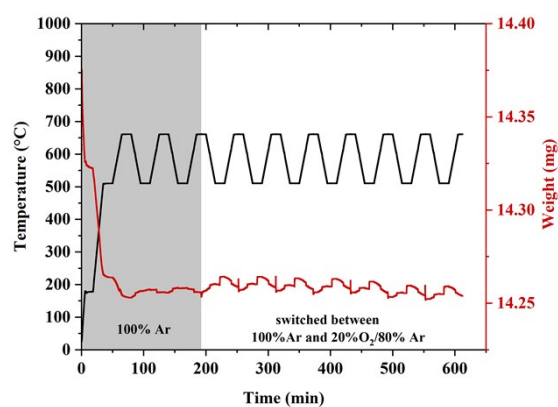
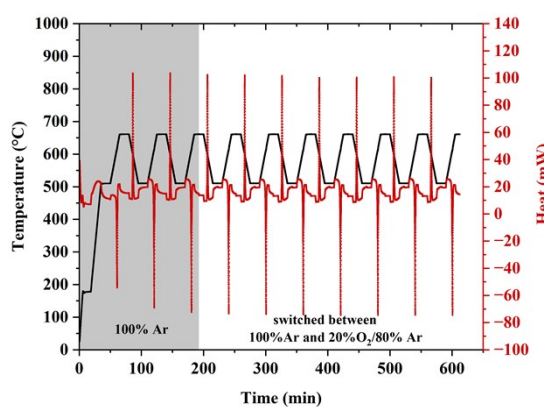
Figure S10. TGA-DSC Measurements for LiF-NaF-CaF₂ at 525-675 °C under 100% Ar (a) Heat Flow (mW) (b) Weight (mg)



(a)

(b)

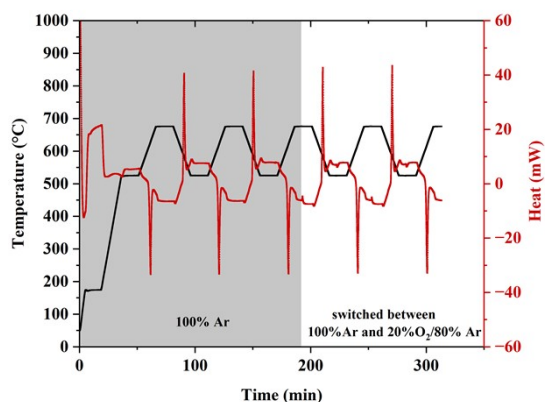
Figure S11. TGA-DSC Measurements for LSF1: LiF-NaF-CaF₂ with the weight ratio of 0.5:0.5 at 525/20%O₂-675 °C/Ar (a) Heat Flow (mW) (b) Weight (mg)



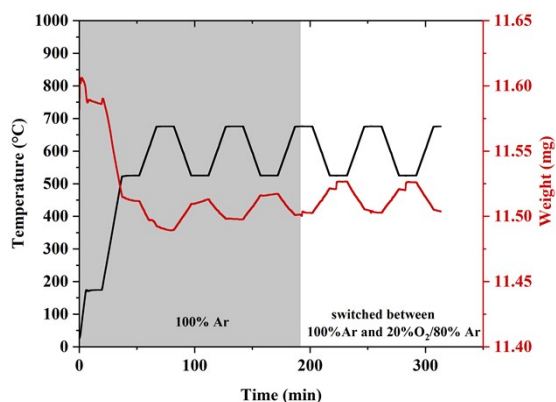
(a)

(b)

Figure S12. TGA-DSC Measurements for LSF1: LiF-NaF-CaF₂ with the weight ratio of 0.4:0.6 at 525/20%O₂-675 °C/Ar (a) Heat Flow (mW) (b) Weight (mg)

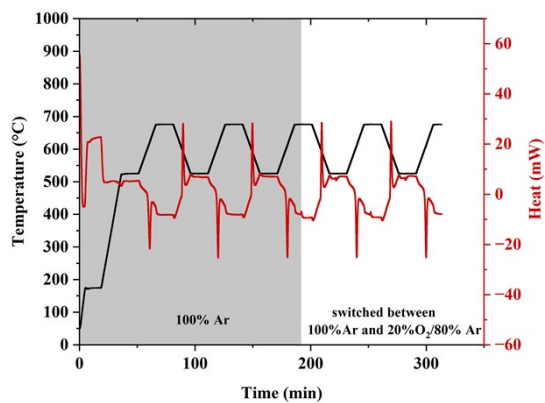


(a)

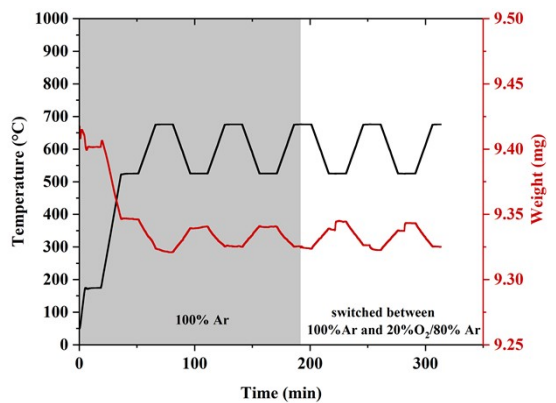


(b)

Figure S13. TGA-DSC Measurements for LSF2: LiF-NaF-CaF₂ with the weight ratio of 0.5:0.5 at 525/20%O₂-675 °C/Ar (a) Heat Flow (mW) (b) Weight (mg)

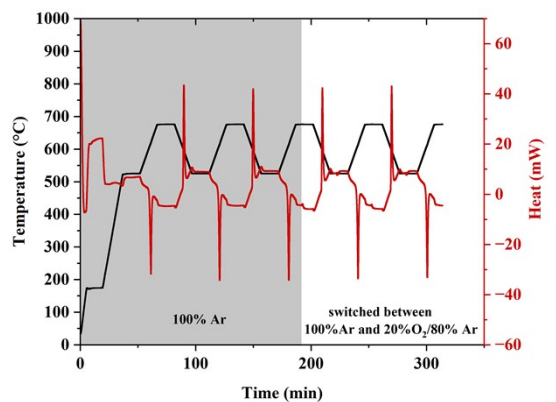


(a)

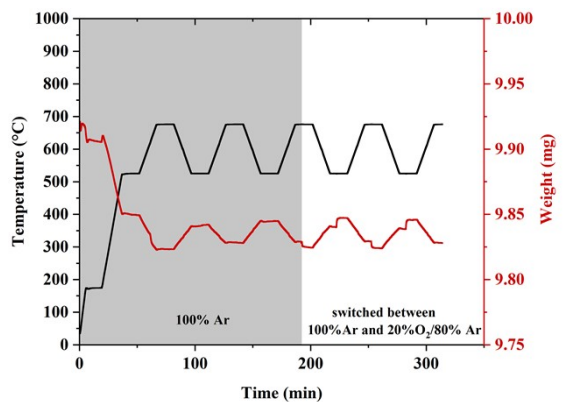


(b)

Figure S14. TGA-DSC Measurements for LSF3: LiF-NaF-CaF₂ with the weight ratio of 0.5:0.5 at 525/20%O₂-675 °C/Ar (a) Heat Flow (mW) (b) Weight (mg)



(a)



(b)

Figure S15. TGA-DSC Measurements for LSCoM2: LiF-NaF-CaF₂ with the weight ratio of 0.5:0.5 at 525/20%O₂-675 °C/Ar (a) Heat Flow (mW) (b) Weight (mg)

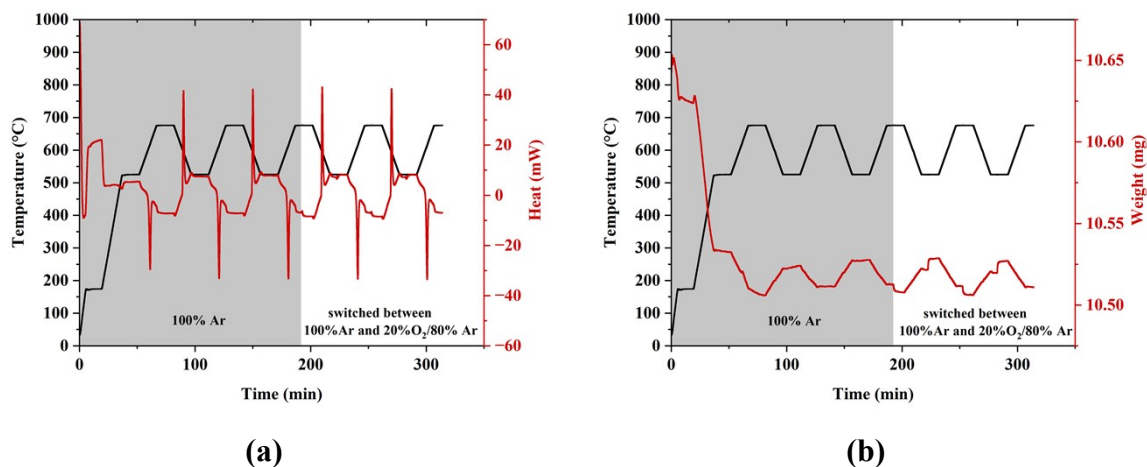


Figure S16. TGA-DSC Measurements for LSFCo: LiF-NaF-CaF₂ with the weight ratio of 0.5:0.5 at 525/20%O₂-675 °C/Ar (a) Heat Flow (mW) (b) Weight (mg)

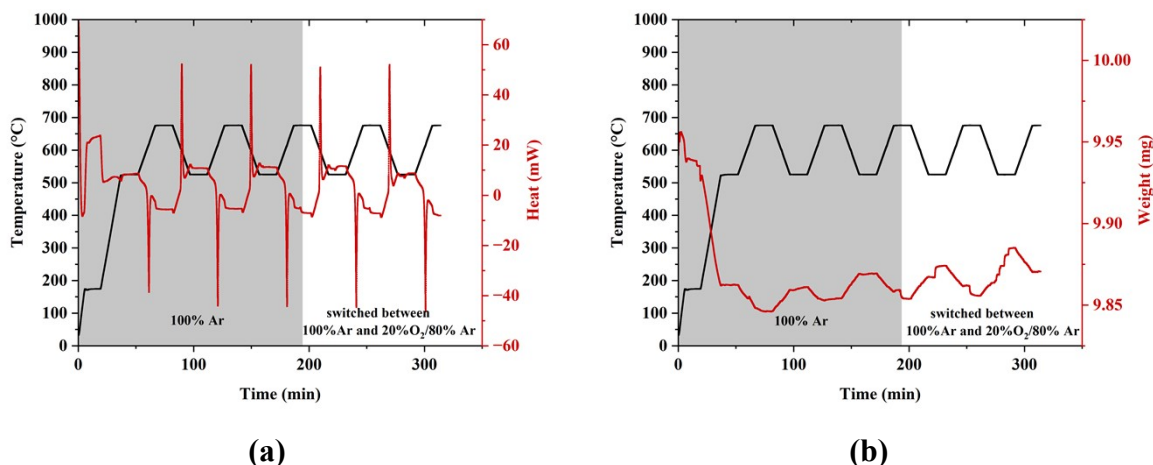


Figure S17. TGA-DSC Measurements for LSFCo: LiF-NaF-CaF₂ with the weight ratio of 0.4:0.6 at 525/20%O₂-675 °C/Ar (a) Heat Flow (mW) (b) Weight (mg)

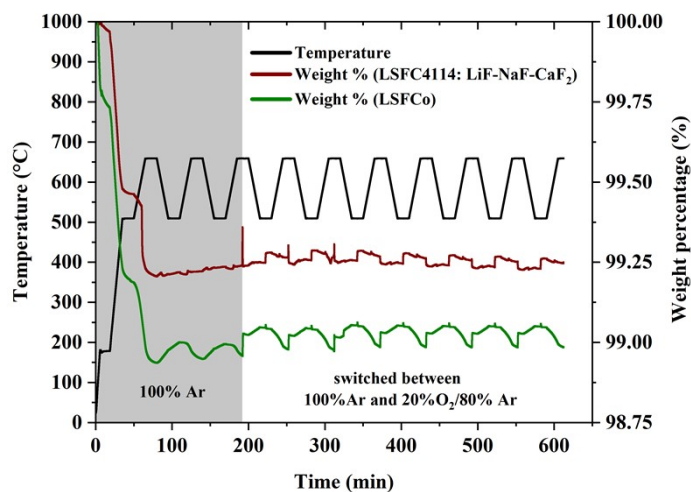


Figure S18. Comparison of weight percentages for LSF_{Co} and LSF_{Co}: LiF-NaF-CaF₂ with the weight ratio of 0.5:0.5 at 510/20%O₂-660 °C/Ar

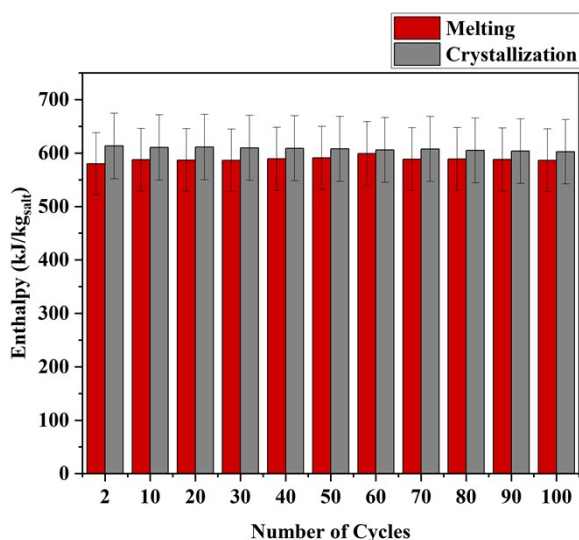


Figure S19. Melting and crystallization enthalpy for LSF1: LiF-NaF-CaF₂ with the weight ratio of 0.4:0.6 at 510 °C/20% O₂-660 °C/Ar during 100 cycles

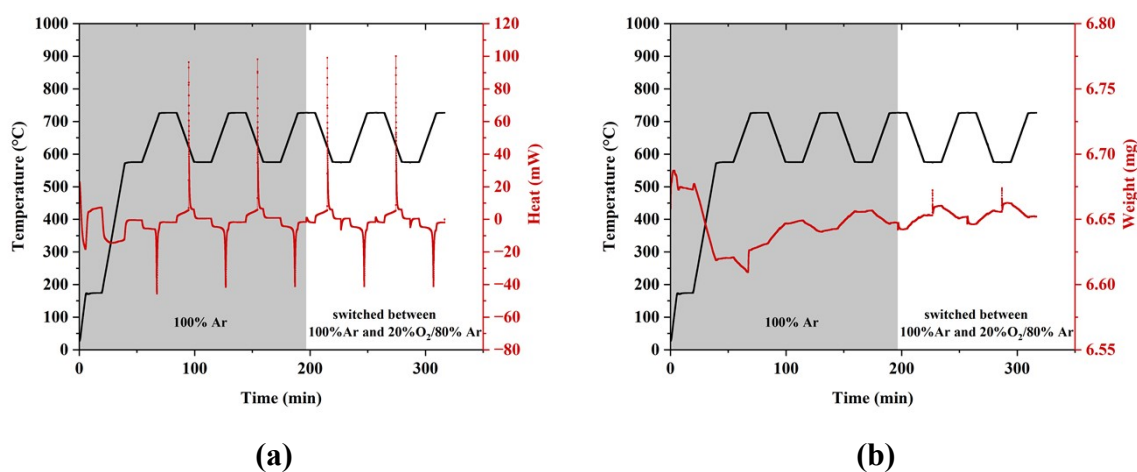
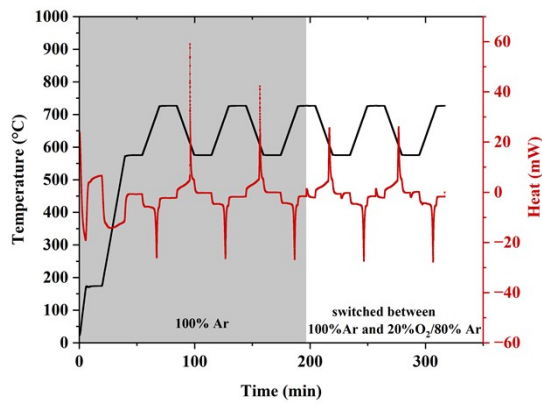
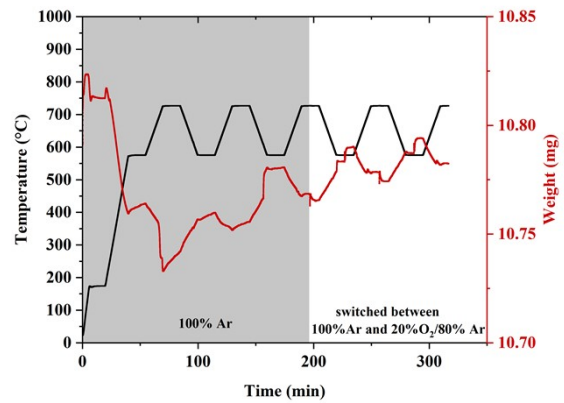


Figure S20. TGA-DSC Measurements for Li₂MoO₄ at 580/20%O₂-730 °C/Ar (a) Heat Flow (mW) (b) Weight (mg)

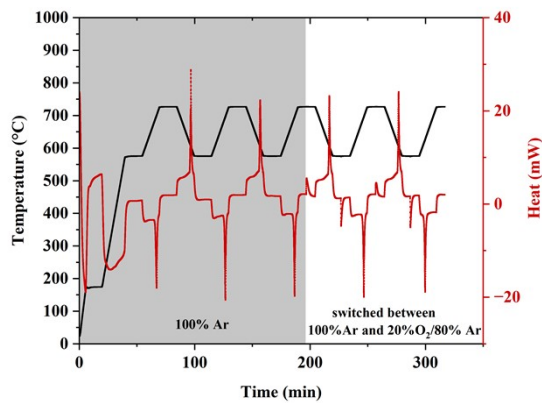


(a)

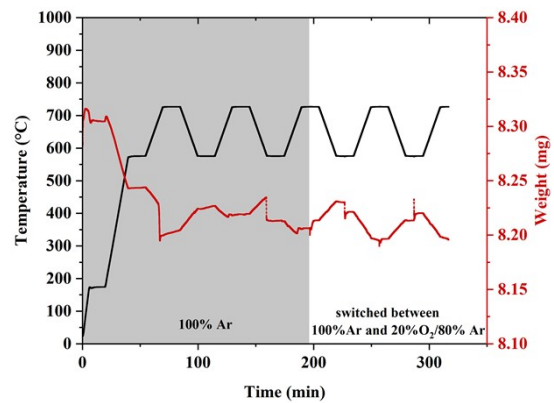


(b)

Figure S21. TGA-DSC Measurements for LSF1:Li₂MoO₄ with the weight ratio of 0.5:0.5 at 580/20%O₂-730 °C/Ar (a) Heat Flow (mW) (b) Weight (mg)

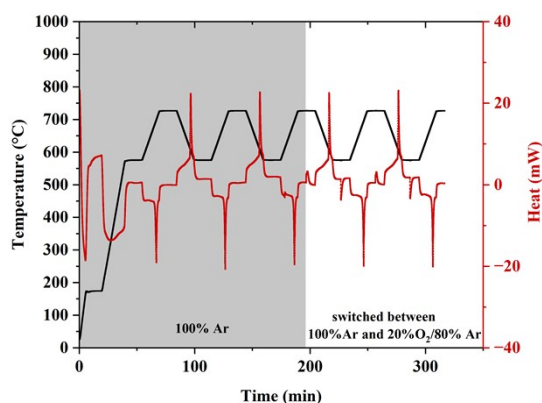


(a)

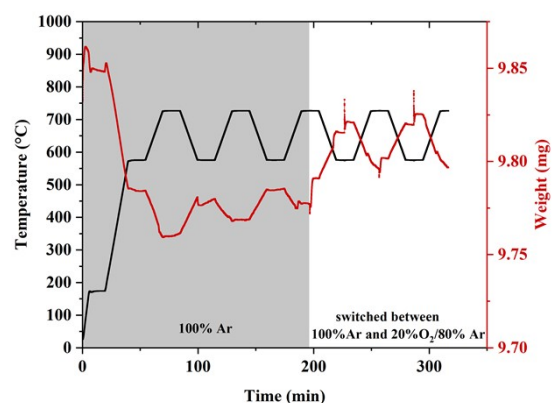


(b)

Figure S22. TGA-DSC Measurements for LSF2:Li₂MoO₄ with the weight ratio of 0.5:0.5 at 580/20%O₂-730 °C/Ar (a) Heat Flow (mW) (b) Weight (mg)



(a)



(b)

Figure S23. TGA-DSC Measurements for LSF2:Li₂MoO₄ with the weight ratio of 0.6:0.4 at 580/20%O₂-730 °C/Ar (a) Heat Flow (mW) (b) Weight (mg)

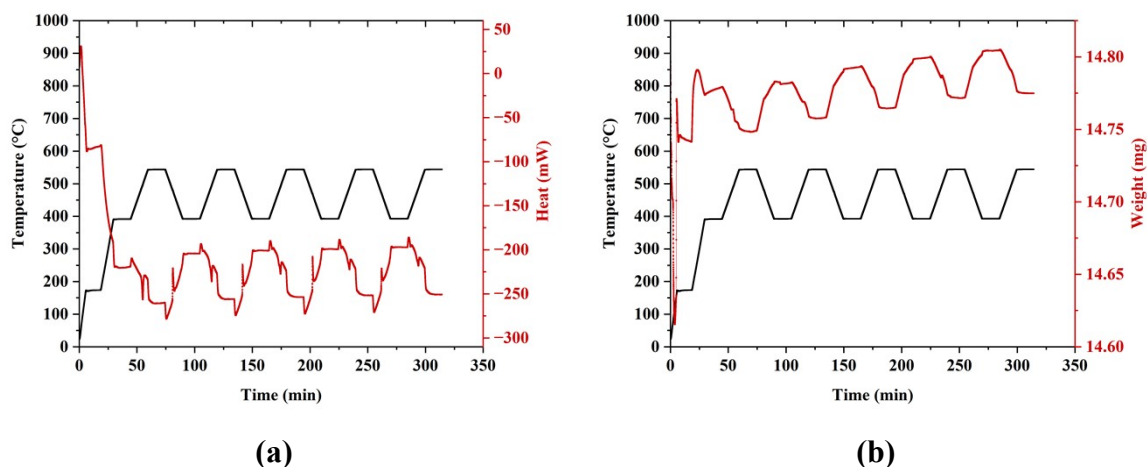


Figure S24. TGA-DSC Measurements for LSF1: $\text{Li}_2\text{CO}_3\text{-Na}_2\text{CO}_3$ with the weight ratio of 0.5:0.5 at 390-540 °C under 50% CO_2 /50%Ar (a) Heat Flow (mW) (b) Weight (mg)

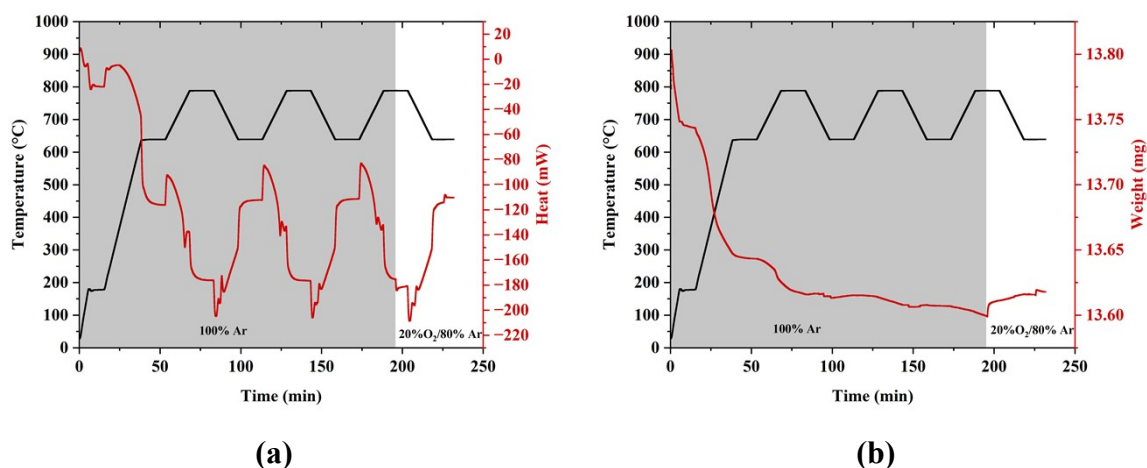


Figure S25. TGA-DSC Measurements for LSF1: $\text{MgF}_2\text{-NaF-CaF}_2$ with the weight ratio of 0.5:0.5 at 640/20% O_2 -790 °C/Ar (a) Heat Flow (mW) (b) Weight (mg)

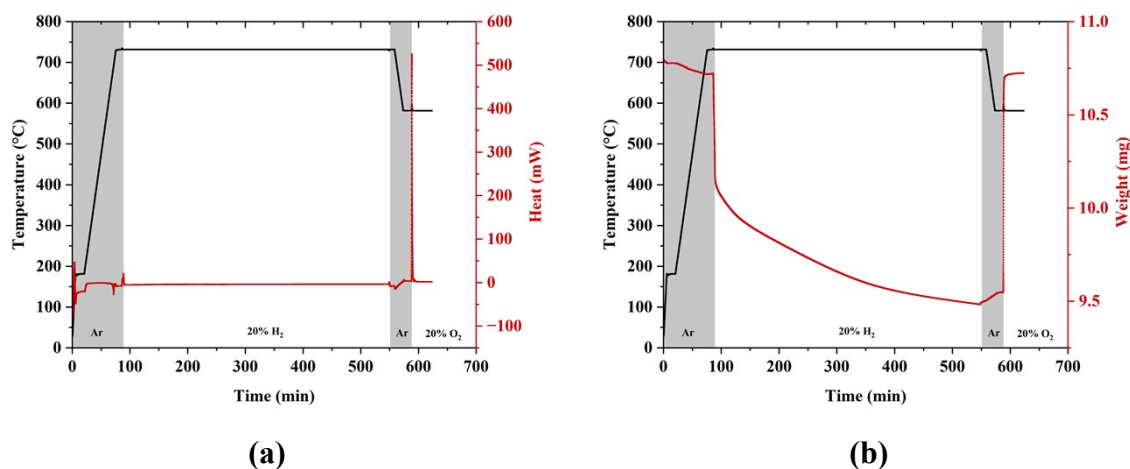
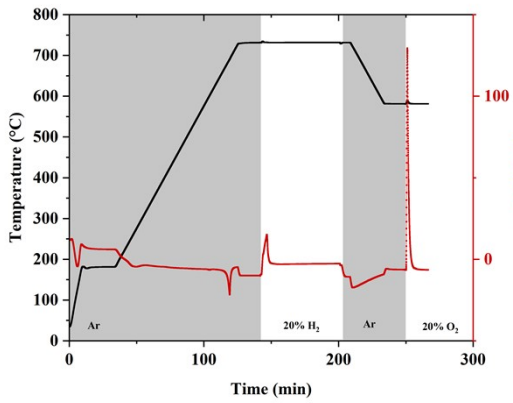
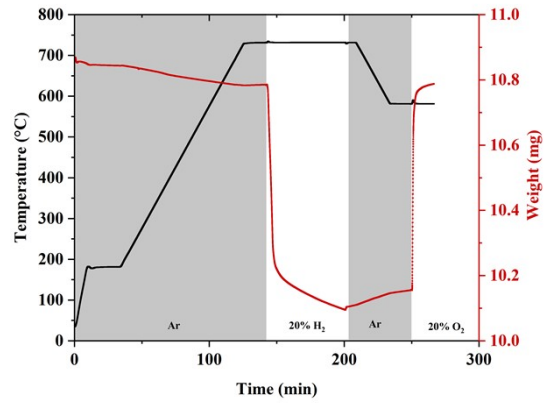


Figure S26. TGA-DSC Measurements with long reduction time for LSF1: Li_2MoO_4 with the weight ratio of 0.5:0.5 at 580/20% O_2 -730 °C/20% H_2 (a) Heat Flow (mW) (b) Weight (mg)

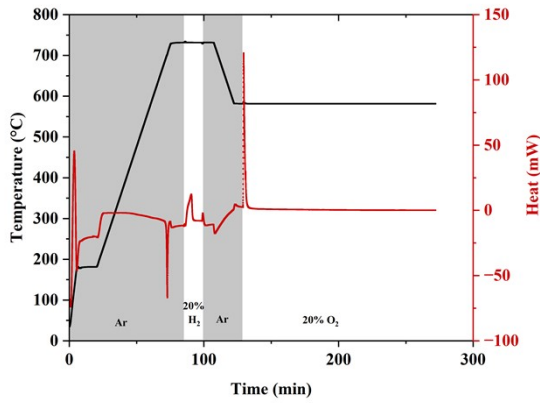


(a)

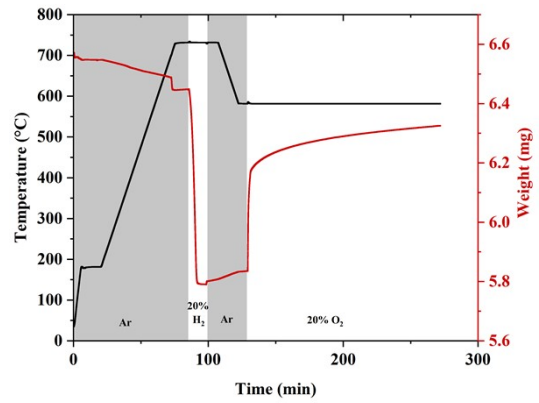


(b)

Figure S27. TGA-DSC Measurements with short reduction time for LSF1: Li_2MoO_4 with the weight ratio of 0.5:0.5 at $580/20\%\text{O}_2\text{-}730^\circ\text{C}/20\%\text{H}_2$ (a) Heat Flow (mW) (b) Weight (mg)

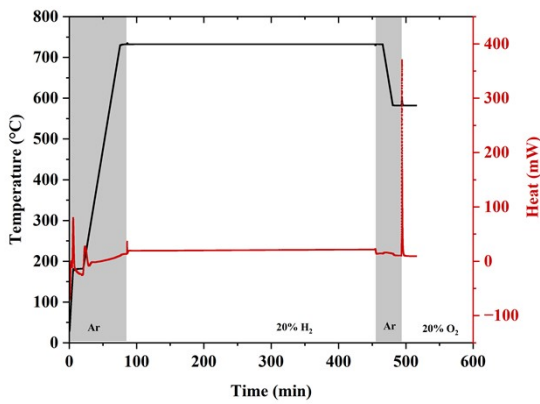


(a)

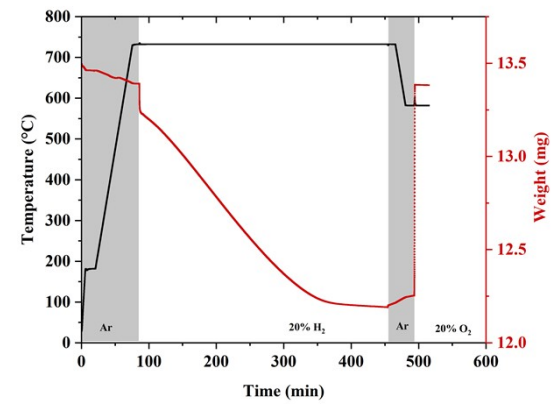


(b)

Figure S28. TGA-DSC Measurements for Li_2MoO_4 at $580/20\%\text{O}_2\text{-}730^\circ\text{C}/20\%\text{H}_2$ (a) Heat Flow (mW) (b) Weight (mg)



(a)



(b)

Figure S29. TGA-DSC Measurements with long reduction time for LSF1 at 580/20%O₂-730 °C/20%H₂ (a) Heat Flow (mW) (b) Weight (mg)

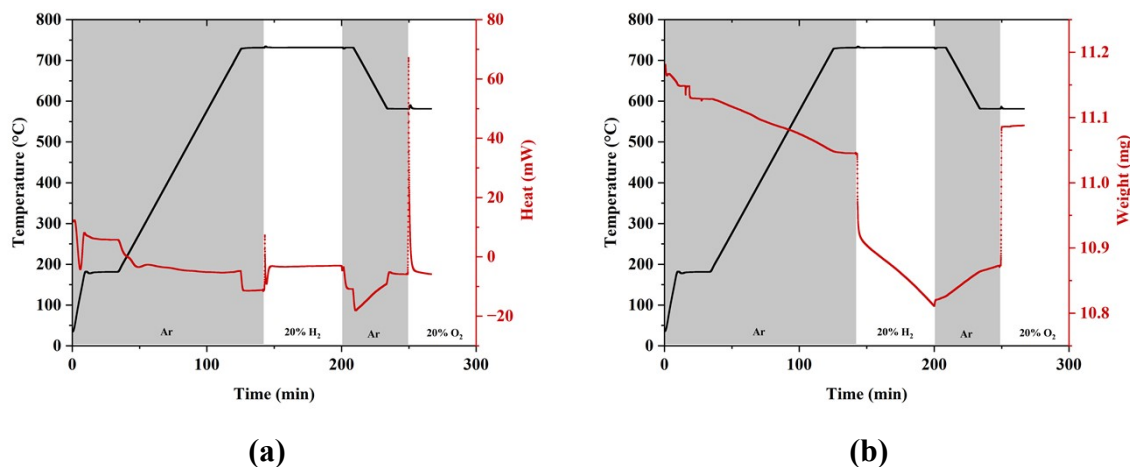


Figure S30. TGA-DSC Measurements with short reduction time for LSF1 at 580/20%O₂-730 °C/20%H₂ (a) Heat Flow (mW) (b) Weight (mg)

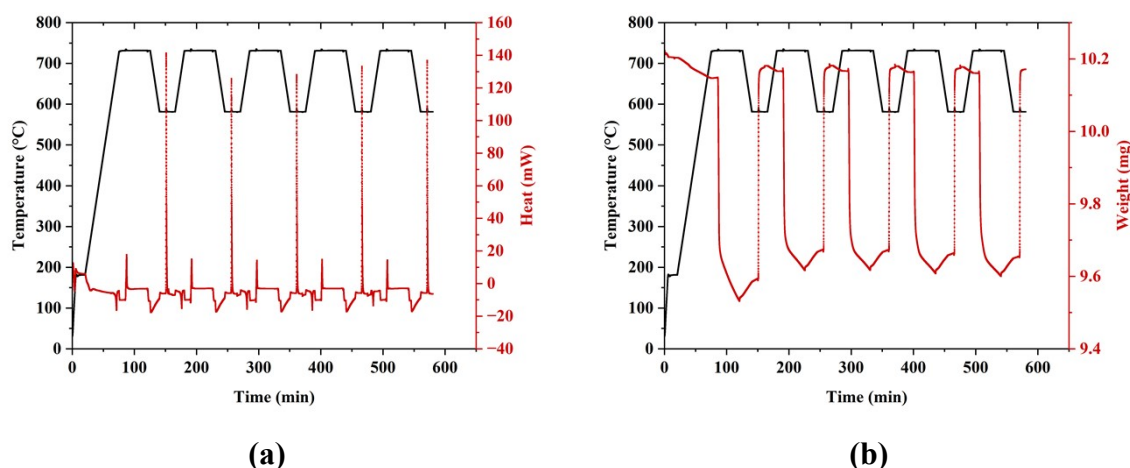


Figure S31. TGA-DSC Measurements with short reduction time for LSF1: Li₂MoO₄ with the weight ratio of 0.6:0.4 at 580/20%O₂-730 °C/20%H₂ for 5 cycles (a) Heat Flow (mW) (b) Weight (mg)

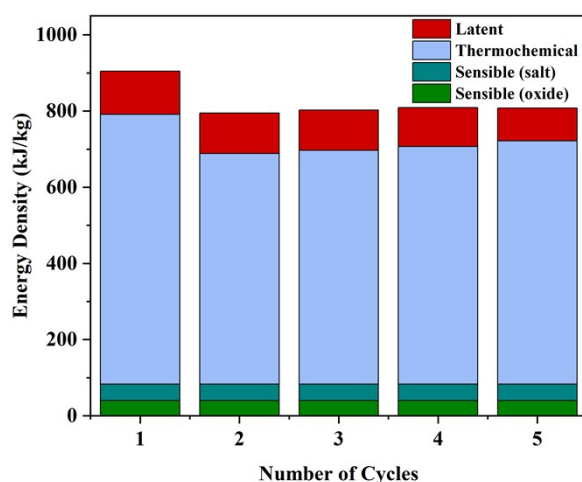


Figure 32 Overall energy density (kJ/kg) for LSF1: Li_2MoO_4 with the weight ratio of 0.6:0.4 at $580/20\%\text{O}_2$ - $730\text{ }^\circ\text{C}/20\%\text{H}_2$ for 5 cycles. Latent heat is the measured melting enthalpy from DSC. Thermochemical heat is measured using DSC during oxidation. Sensible heat is based on estimated heat capacities through additive principle using NIST database⁹

Table S2. Measured melting/crystallization enthalpy ($\text{kJ}/\text{kg}_{\text{salt}}$) and melting/crystallization points ($^\circ\text{C}$) of composite materials. The weight ratios of eutectic salt mixtures are provided in Table 2. Melting/Crystallization enthalpies and temperatures were determined from the second cycles.

Sample Name (weight ratio)	Melting Enthalpy ($\text{kJ}/\text{kg}_{\text{salt}}$) $\pm 10\%$	Melting Temperature ($^\circ\text{C}$)	Crystallization Enthalpy ($\text{kJ}/\text{kg}_{\text{salt}}$) $\pm 10\%$	Crystallization Temperature ($^\circ\text{C}$)
LiF-NaF-CaF ₂	622.93	609.69	620.26	612.76
Li ₂ MoO ₄	281.49	693.40	261.94	627.05
NaF-CaF ₂	561.80	804.67	580.26	808.02
NaF- CaF ₂ :SCFM2 (0.4:0.6)	532.47	797.91	467.41	804.93
LSCoM2: LiF- NaF-CaF ₂ (0.5:0.5)	549.55	605.17	582.95	604.55
LSF1: LiF-NaF- CaF ₂ (0.5:0.5)	542.73	603.36	569.61	608.46
LSF1: LiF-NaF- CaF ₂ (0.4:0.6)	579.74	606.66	613.30	613.21
LSF2: LiF-NaF- CaF ₂ (0.5:0.5)	544.00	600.06	552.48	602.44
LSFCo: LiF- NaF-CaF ₂ (0.5:0.5)	537.41	602.98	553.08	602.66
LSFCo: LiF- NaF-CaF ₂	595.05	606.73	617.56	606.00

(0.4:0.6)				
LSF3: LiF-NaF- CaF₂ (0.5:0.5)	466.54	600.88	480.76	602.37
LSF1: Li₂MoO₄(0.5:0.5)	254.59	685.08	244.19	616.09
LSF2: Li₂MoO₄(0.5:0.5)	252.46	687.55	236.08	615.98
LSF2: Li₂MoO₄(0.6:0.4)	219.95	688.18	211.47	613.46
LSF1: Li₂CO₃- Na₂CO₃ (0.5:0.5)	222.79	482.80	238.75	478.85
SCFM2: NaF- NaCl (0.5:0.5)	340.84	672.13	332.96	690.45
SF: LiF-NaF (0.5:0.5)	489.30	615.28	514.91	621.84
SBF: LiF-NaF (0.5:0.5)	597.57	603.74	672.85	615.49

4. Post-experimental XRD:

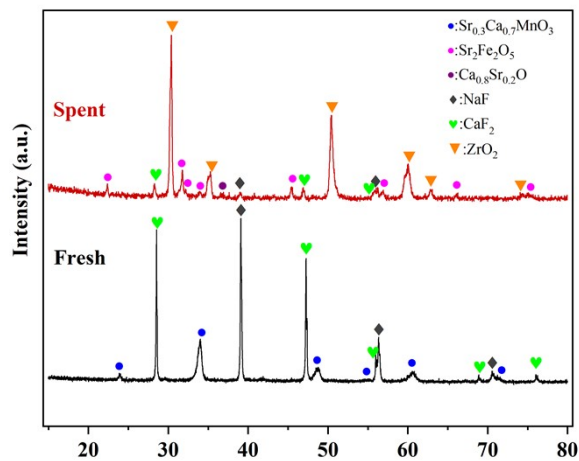


Figure S33. Comparison of fresh and spent (after 100 cycles between 670°C/20% O₂-820°C/Ar) SCFM2:NaF-CaF₂ (0.4:0.6) There is some uncertainty in identifying the minor peak as the Ca_{0.8}Sr_{0.2}O phase as the peak intensities for the composite material are relatively low due to the presence of inert YSZ, which could not be separated from the composite after the experiment.

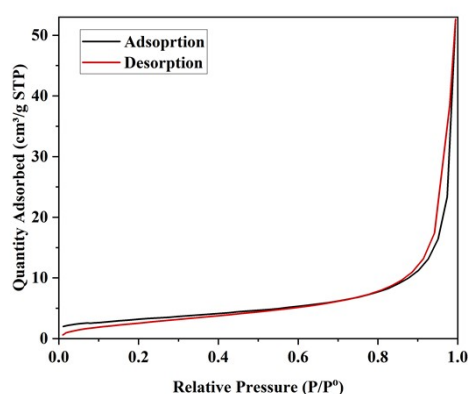
5. Results related to micro-structure of oxide and composite materials:

In the long-run test, porous perovskite oxide particles were used in the composite materials. The porous structures were formed by applying the salt grinding method, which notably increased the S_{BET} from 2.23 m²/g to 11.10 m²/g, as presented in Table S3, and also enlarged pore width and volume. Although the sharp increase at high P/P^0 in the adsorption isotherm curve (Figure S34a) indicates that the material is macroporous²², the BET method was selected for surface area measurement. This surface area obtained via this method primarily accounts for mesopores (2-50nm) which can provide better support by providing favorable capillary

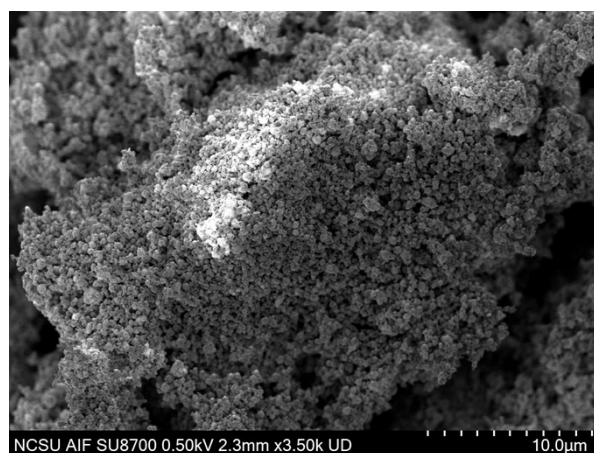
force to avoid salt leakage.²³ The porous structure of salt-grinded LSF1 can be seen in Figure 34b.

Table S3. Comparison of S_{BET} (m^2/g), pore width (nm) and pore volume (m^3/g) before and after the application of salt-grinding method

Sample	S_{BET} (m^2/g)	Average pore width (nm)	Pore Volume (m^3/g)
LSF1	2.23	16.07	0.009
Salt-grinded LSF1	11.41	28.56	0.081



(a)



(b)

Figure S34. For salt-grinded LSF1 (a) Adsorption/desorption isotherm (b) SEM image

The ratio selection for the long-term tests of SCFM2:NaF-CaF₂ and LSF1: NaF-CaF₂-LiF were made by visual inspection of the pellets with 50, 60, and 70% salt ratios. When the salt percentage was above 60%, cracks and salt leakage were seen in the pellets of both composites. Therefore, 60% salt and 40% oxide were used for the sake of stability in the long-term experiments. The demonstration for the pellets of LSF1: NaF-CaF₂-LiF is provided in Figure S35.

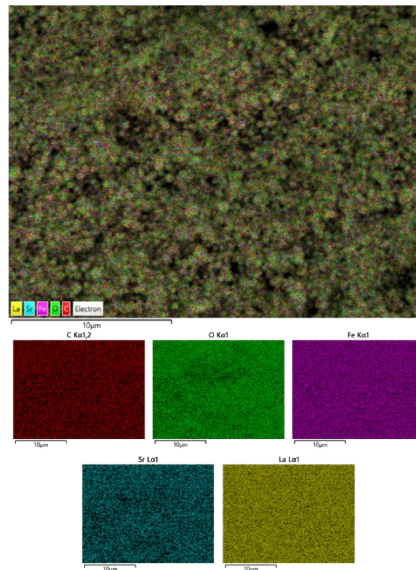


(a)

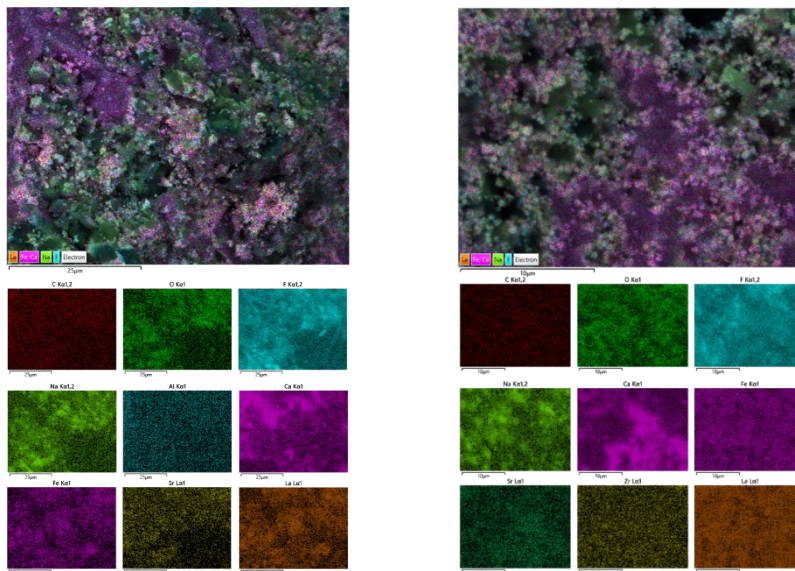


(b)

Figure 35. The samples of LSF1: NaF-CaF₂-LiF with the mass ratios of 0.5:0.5, 0.4:0.6, and 0.3:0.7 from left to right, respectively (a) Before sintering (b) After sintering at 660 °C



(a)



(b)

(c)

Figure S36. EDX images of (a) porous LSF1 after applying the salt grinding method (b) LSF1: LiF-NaF-CaF₂ (0.4:0.6) after sintering, which corresponds to the morphology of composite material after 1 cycle (c) LSF1: LiF-NaF-CaF₂ (0.4:0.6) after 100 cycles

Footnotes

†: School of Mechanical Engineering, Shanghai Jiao Tong University, 800 Dongchuan RD. Minhang District, Shanghai, China

References:

- (1) Pechini, M. P. Method of Preparing Lead and Alkaline Earth Titanates and Niobates and Coating Method Using the Same to Form a Capacitor Images. US3330697A, 1967.
- (2) Ghanbari, E.; Picken, S. J.; Van Esch, J. H. Analysis of Differential Scanning Calorimetry (DSC): Determining the Transition Temperatures, and Enthalpy and Heat Capacity Changes in Multicomponent Systems by Analytical Model Fitting. *J. Therm. Anal. Calorim.* **2023**, *148* (22), 12393–12409. <https://doi.org/10.1007/s10973-023-12356-1>.
- (3) Gunaratne, L. M. W. K.; Shanks, R. A.; Amarasinghe, G. Thermal History Effects on Crystallisation and Melting of Poly(3-Hydroxybutyrate). *Thermochim. Acta* **2004**, *423* (1–2), 127–135. <https://doi.org/10.1016/j.tca.2004.05.003>.
- (4) Menczel, J. D.; Andre, R.; Kohl, W. S.; Krongauz, V. V.; Lőrinczy, D.; Reading, M.; Grebowicz, J. Fundamentals of DSC. In *The Handbook of Differential Scanning Calorimetry*; Elsevier, 2023; pp 1–189. <https://doi.org/10.1016/B978-0-12-811347-9.00005-9>.
- (5) Cai, R.; Bektas, H.; Wang, X.; McClintock, K.; Teague, L.; Yang, K.; Li, F. Accelerated Perovskite Oxide Development for Thermochemical Energy Storage by a High-Throughput Combinatorial Approach. *Adv. Energy Mater.* **2023**, *13* (18), 2203833. <https://doi.org/10.1002/aenm.202203833>.
- (6) Imponenti, L.; Albrecht, K. J.; Braun, R. J.; Jackson, G. S. Measuring Thermochemical Energy Storage Capacity with Redox Cycles of Doped-CaMnO₃. *ECS Trans.* **2016**, *72* (7), 11–22. <https://doi.org/10.1149/07207.0011ecst>.
- (7) Khokhlov, V.; Ignatiev, V.; Afonichkin, V. Evaluating Physical Properties of Molten Salt Reactor Fluoride Mixtures. *J. Fluor. Chem.* **2009**, *130* (1), 30–37. <https://doi.org/10.1016/j.jfluchem.2008.07.018>.
- (8) Li, Y.; Xu, X.; Wang, X.; Li, P.; Hao, Q.; Xiao, B. Survey and Evaluation of Equations for Thermophysical Properties of Binary/Ternary Eutectic Salts from NaCl, KCl, MgCl₂, CaCl₂, ZnCl₂ for Heat Transfer and Thermal Storage Fluids in CSP. *Sol. Energy* **2017**, *152*, 57–79. <https://doi.org/10.1016/j.solener.2017.03.019>.
- (9) Chase, M., Jr. *NIST-JANAF Thermochemical Tables, Fourth Edition*; American Chemical Society: Washington DC, 1998; Vol. 9.
- (10) Williams, D. F. *Assessment of Candidate Molten Salt Coolants for the Advanced High Temperature Reactor (AHTR)*; ORNL/TM-2006/12, 885975; 2006; p ORNL/TM-2006/12, 885975. <https://doi.org/10.2172/885975>.
- (11) Matskevich, N. I.; Shlegel, V. N.; Sednev, A. L.; Semerikova, A. N.; Zaitsev, V. P.; Kuznetsov, V. A.; Novikov, A. Yu.; Zuev, A. Yu. Thermodynamic Characteristics of Li₂MoO₄, Li₂W_{0.85}Mo_{0.15}O₄ Single Crystals and Stability Direction for Alkali

- Molybdates. *J. Chem. Thermodyn.* **2020**, *143*, 106059.
<https://doi.org/10.1016/j.jct.2020.106059>.
- (12) Zhang, H.; Li, M.-J.; Fang, W.-Z.; Dan, D.; Li, Z.-Y.; Tao, W.-Q. A Numerical Study on the Theoretical Accuracy of Film Thermal Conductivity Using Transient Plane Source Method. *Appl. Therm. Eng.* **2014**, *72* (1), 62–69.
<https://doi.org/10.1016/j.applthermaleng.2014.01.058>.
- (13) Zhang, H.; Jin, Y.; Gu, W.; Li, Z. Y.; Tao, W. Q. A Numerical Study on the Influence of Insulating Layer of the Hot Disk Sensor on the Thermal Conductivity Measuring Accuracy. *Prog. Comput. Fluid Dyn. Int. J.* **2013**, *13* (3/4), 191.
<https://doi.org/10.1504/PCFD.2013.053660>.
- (14) Zheng, Q.; Kaur, S.; Dames, C.; Prasher, R. S. Analysis and Improvement of the Hot Disk Transient Plane Source Method for Low Thermal Conductivity Materials. *Int. J. Heat Mass Transf.* **2020**, *151*, 119331.
<https://doi.org/10.1016/j.ijheatmasstransfer.2020.119331>.
- (15) Stølen, S.; Grønvold, F.; Brinks, H.; Atake, T.; Mori, H. Heat Capacity and Thermodynamic Properties of LaFeO₃ and LaCoO₃ from T=13 K to T=1000 K. *J. Chem. Thermodyn.* **1998**, *30* (3), 365–377. <https://doi.org/10.1006/jcht.1997.0309>.
- (16) Parida, S. C.; Singh, Z.; Dash, S.; Prasad, R.; Venugopal, V. Thermodynamic Studies on LaFeO₃(s). *J. Alloys Compd.* **1998**, *280* (1–2), 94–98. [https://doi.org/10.1016/S0925-8388\(98\)00699-9](https://doi.org/10.1016/S0925-8388(98)00699-9).
- (17) Jain, A.; Ong, S. P.; Hautier, G.; Chen, W.; Richards, W. D.; Dacek, S.; Cholia, S.; Gunter, D.; Skinner, D.; Ceder, G.; Persson, K. A. Commentary: The Materials Project: A Materials Genome Approach to Accelerating Materials Innovation. *APL Mater.* **2013**, *1* (1), 011002. <https://doi.org/10.1063/1.4812323>.
- (18) Bartel, C. J. Review of Computational Approaches to Predict the Thermodynamic Stability of Inorganic Solids. *J. Mater. Sci.* **2022**, *57* (23), 10475–10498.
<https://doi.org/10.1007/s10853-022-06915-4>.
- (19) Misra, A. K. Fluoride Salts as Phase Change Materials for Thermal Energy Storage in the Temperature Range 1000–1400 K: Thermal Analysis and Heat of Fusion Measurements. *J. Electrochem. Soc.* **1988**, *135* (4), 850–854.
<https://doi.org/10.1149/1.2095808>.
- (20) Kenisarin, M. M. High-Temperature Phase Change Materials for Thermal Energy Storage. *Renew. Sustain. Energy Rev.* **2010**, *14* (3), 955–970.
<https://doi.org/10.1016/j.rser.2009.11.011>.
- (21) Wang, T.; Mantha, D.; Reddy, R. G. Novel High Thermal Stability LiF–Na₂CO₃–K₂CO₃ Eutectic Ternary System for Thermal Energy Storage Applications. *Sol. Energy Mater. Sol. Cells* **2015**, *140*, 366–375. <https://doi.org/10.1016/j.solmat.2015.04.033>.
- (22) Thommes, M.; Kaneko, K.; Neimark, A. V.; Olivier, J. P.; Rodriguez-Reinoso, F.; Rouquerol, J.; Sing, K. S. W. Physisorption of Gases, with Special Reference to the Evaluation of Surface Area and Pore Size Distribution (IUPAC Technical Report). *Pure Appl. Chem.* **2015**, *87* (9–10), 1051–1069. <https://doi.org/10.1515/pac-2014-1117>.
- (23) Qian, T.; Li, J.; Min, X.; Deng, Y.; Guan, W.; Ning, L. Diatomite: A Promising Natural Candidate as Carrier Material for Low, Middle and High Temperature Phase Change Material. *Energy Convers. Manag.* **2015**, *98*, 34–45.
<https://doi.org/10.1016/j.enconman.2015.03.071>.